Korean J. Chem. Eng., 40(4), 986-998 (2023)
DOI: 10.1007/s11814-022-1280-3

pISSN: 0256-1115
eISSN: 1975-7220

Amorphous solid dispersions of tegoprazan and three different polymers: *In vitro/in vivo* evaluation of physicochemical properties

Paul Kim*, In-Seo Lee*, Ji-Yoon Kim*, Min-Jeong Lee, and Guang Jin Choi*,**,†**

*Department of Medical Science, Soonchunhyang University, Asan, Chungnam 31538, Korea
**Department of Pharmaceutical Engineering, Soonchunhyang University, Asan, Chungnam 31538, Korea
(*Received 10 June 2022 • Revised 11 August 2022 • Accepted 1 September 2022*)

Abstract−Polymer-based amorphous solid dispersion (PASD) technology has attracted attention as one of the most feasible approaches for improving the solubility, dissolution rate, and bioavailability of insoluble drugs. Tegoprazan (TPZ) is a promising new drug used to treat gastroesophageal reflux disease with poor water solubility (~0.03 mg/mL). This study developed novel PASD materials containing TPZ. Three polymers were used for this study: PVP, HPMCAS, and carbomer. The PASD powders were prepared via solvent evaporation at 50% drug loading. The physicochemical properties of PASD solids were characterized using PXRD, MDSC, TGA, FT-IR, 1H SS-NMR, and stability testing. PASD powders fabricated with the neutral polymer PVP showed poor stability against drug crystallization. In contrast, those prepared using HPMCAS and carbomer showed no signs of crystallization even after three months of storage at 40oC/75% RH. A correlation between intermolecular interaction and physical stability was inferred for the TPZ PASD formulations. Amorphization of the crystalline TPZ with HPMCAS and carbomer resulted in a greatly increased in vitro dissolution rate. These two polymers showed similar performance, eliciting appreciable improvement in the in vivo absorption tests in rats. In summary, PASD formulations using acidic polymers (HPMCAS and carbomer) are novel formulations for improving the therapeutic effects of TPZ.

Keywords: Tegoprazan, Polymer-based Amorphous Solid Dispersion, Drug-polymer Interaction, *In Vivo* Absorption, Glass Transition Temperature

INTRODUCTION

Amorphous solid dispersions (ASDs) are solid materials in which drug molecules are dispersed predominantly in an amorphous form within an excipient matrix [1]. Extensive efforts have been devoted to understanding and applying ASD technologies in academic and industrial settings. Many articles on ASDs can be found in various academic publications, supporting the strong trend toward ASD-based technology to address the challenges in pharmaceutical formulation development. Almost all comprehensive reviews have been published recently [2-5]. These reviews report on enhancing the solubility/dissolution of drug molecules and optimizing their formulations with the desired physical stability against crystallization. According to a recent survey, over 40 innovator drugs have been approved for ASD formulations annually in the US, EU, and Japan since 2018 [3]. This implies that the industrial sector has accepted the maturity and robustness of ASD technologies.

Pharmaceutical amorphous solids are generally divided into three categories: polymer-based ASDs (PASDs), mesoporous silica-based ASDs, and coamorphous materials [6]. Few studies on mesoporous silica-based ASDs have been conducted [7-9], but interest in this approach is increasing. In each study, the roles of the silanol functionalities in direct contact with drug molecules were pivotal to the stability of the amorphous phases, especially at higher drug loading [8]. Coamorphous materials, in which amorphous drug molecules are stabilized low-molecular-weight compounds instead of polymers, are anticipated to offer a few potential advantages over other ASD approaches. First, a drug loading higher than 50 wt% could be feasible depending on the intermolecular interactions present. The common problem regarding the hygroscopicity of PASDs with hydrophilic polymers might be alleviated by coamorphous material approaches [6].

Since many drugs in the PASD form appear on the market each year, it is evident that PASD formulations have become dominant in the field of pharmaceuticals. Despite enormous efforts for their long-term development, PASDs have a few disadvantages, including low drug-loading capability. In addition, some polymers, such as polyvinylpyrrolidone (PVP), whose glass transition temperature is high, are hygroscopic. Furthermore, their long-term stability under water-containing conditions is expected to be poor [10]. Strong drug-polymer intermolecular interactions effectively inhibit the recrystallization of APIs in the solid dispersion and lead to a relatively stable PASD system with high drug loading capacity [11-16]. Polymers containing strong proton donors (e.g., polyacrylic acid [PAA]) effectively disrupt the molecular self-assembly of alkaline drugs containing an amide group. In contrast, polymers containing strong proton acceptors (e.g., PVP) exert a similar effect on acidic drugs [17-20]. Hydroxypropyl methylcellulose acetate succinate (HPMCAS) is also a promising polymer that can form molecular interactions with drugs, which affects the stability of the amor-

†To whom correspondence should be addressed.
E-mail: guangchoi@gmail.com

phized drug in the dispersion [21-23].

As physical stability is the primary concern in ASD formulations, the characterization, detection, and quantification of the signs and/or extent of phase transition from the amorphous state to crystallinity should be performed within expectations [4]. Material characterization should be performed at the molecular and particulate levels [24]. Fourier-transform infrared (FT-IR) and solid-state nuclear magnetic resonance (SS-NMR) spectroscopy are the most widely used analytical tools for the molecular characterization of ASD systems [25,26]. In contrast, powder X-ray diffraction (PXRD), differential scanning calorimetry (DSC), and thermogravimetric analysis (TGA) are the most popular techniques for characterizing ASDs on a particulate scale.

Even though a low degree of crystallization in ASDs plays an important role in the performance of the resulting solid materials, PXRD, DSC, and FT-IR will not work satisfactorily when the physicochemical change in the amorphous structure is not significant. For instance, PXRD and DSC cannot detect or quantify the existence of crystalline materials, typically on the order of 1-5%. Recently, the application of transmission electron microscopy for extremely low levels of crystallinity in ASDs has been reported [27]. Efforts have been made to qualitatively and quantitatively characterize the amorphous state of PASD materials. Among them, total diffraction analysis (TDA) and pair distribution function (PDF) analyses were employed to understand amorphous structures that were undetectable using single-crystal or PXRD measurements. The width of the X-ray amorphous halos can be utilized to determine the extent of departure from random packing for a given PASD specimen. As introduced at Triclic Labs, the Debye diffraction theory and continuous structure factor are required for a more detailed analysis.

Gastroesophageal reflux disease (GERD) and other related diseases have been widely treated using proton pump inhibitors (PPIs). PPIs elicit their long-lasting effects against gastric acid production by inhibiting the H^+/K^+-ATPase enzyme system on the surface of parietal cells. Due to the insufficient effectiveness of most PPIs in ultra-rapid metabolizers and the slow effect, a new class of drugs called potassium-competitive acid blockers (P-CABs) has emerged to competitively block the potassium-binding site of the gastric H^+/K^+-ATPase. After the first-in-class P-CAB vonoprazan was approved in Japan in 2015 [28], tegoprazan (TPZ) appeared as a promising P-CAB with comparable therapeutic efficacy but with fewer side effects [29,30]. TPZ was approved for the treatment of GERD in South Korea in 2018 and is expected to be approved by the US FDA soon. The mean half-life ($t_{1/2}$) of TPZ is known to be 3.7-6.2 h; the apparent clearance (CL/F), including volume of distribution (Vd), was reported to be approximately 17.6 L/h and 107.9 L, respectively [29,31,32]. According to the TPZ patent for its crystalline form [33], stability was greatly improved in crystal form A. Nevertheless, its solubility remained extremely low (~30 μg/mL); thus, its bioavailability should be improved. Several solid salt forms have been reported in a subsequent patent [34], demonstrating a significant improvement in aqueous solubility. However, some salt materials with outstanding solubility showed weaknesses in solid stability under humid conditions. Therefore, novel solid materials are required to solve these solubility and stability issues.

This study applied the PASD approach to the new drug TPZ to enhance its *in vitro* dissolution and *in vivo* absorption behaviors using two acidic polymers, cross-linked polyacrylic acid (carbomer) and HPMCAS-LF. We also evaluated the molecular interactions between TPZ and three polymers (HPMCAS, carbomer, and PVP) in PASD systems based on molecular characterization in the solid state, such as modulated-differential scanning calorimetry (MDSC), attenuated total reflectance (ATR) FT-IR, and ^{1}H SS-NMR, and assessed the physical stability of the three PASD systems against crystallization. The experimental procedures and physicochemical characterization results are presented in detail, revealing a feasible PASD solid material that enhanced the therapeutic effect of TPZ.

EXPERIMENTS

1. Materials

TPZ (99%) was supplied by Changzhou SYM-Tech Co. (Beijing, China). HPMCAS grade LF (HPMCAS-LF; 99%), which has the highest succinoyl and lowest acetyl substitution and the most acidic HPMCAS available commercially [35], was donated by Shin-Etsu Chemical Co. (Tokyo, Japan). Carbomer (Carbopol 981; 99%) was provided by Hannong Chemicals (Gyeonggi-do, Korea). PVP K90 (99%) was purchased from Millipore-Sigma (Burlington, MA, USA). The chemical structures of TPZ and the three polymers are illustrated in Fig. S1.

2. Sample Preparation

PASD materials are typically produced in three ways: via solvent evaporation, energy milling, or co-melting. Our PASD powders were prepared using the solvent evaporation method primarily due to the high melting point of TPZ, which is 223.5 °C. Every PASD material was checked for an amorphized dispersion structure via PXRD or other methods. Two grams of TPZ and each polymer were dissolved in 500 mL methanol until a clear solution was obtained. Each solution was then filtered using a 0.45 μm nylon filter (Whatman, Marlborough, MA) and subjected to solvent evaporation using a rotary evaporator (Rotavapor R-210, Buchi, Flawil, Switzerland). This rotavap process was typically completed after 10 minutes. The resulting products were vacuum-dried overnight to remove the residual solvent. The PASD powders were stored in a desiccator until further characterization.

3. Theoretical Consideration

The predicted glass transition temperature ($T_g^{m\text{-}calc}$) of the amorphous solid dispersion was calculated using the Gordon-Taylor equation [36] as described below:

$$T_g^{m\text{-}calc} = \frac{(w_1 T_{g1} + k w_2 T_{g2})}{(w_1 + k w_2)} \quad (1)$$

where w_1 and w_2 are the API and polymer mass fraction, respectively, T_{g1} is the glass transition temperature of the drug, and T_{g2} is the glass transition temperature for each polymer. The constant k is an adjustable fitting parameter and is calculated using Eq. (2) from the densities of the drug and the polymer, denoted as ρ_1 and ρ_2, respectively.

$$k = \frac{T_{g1}\rho_1}{T_{g2}\rho_2} \quad (2)$$

The Hildebrand solubility parameter, δ, is defined as the energy

per unit volume required to break intermolecular bonds and vaporize one mole of molecules from the liquid phase [37]. It is estimated using Eq. (3) as follows:

$$\delta = \sqrt{\frac{\Delta H_{vap} - RT}{V_m}} \quad (3)$$

where ΔH_{vap} is the enthalpy of vaporization associated with the phase change (from the liquid phase to the gas phase), R is the ideal gas constant, T is the absolute temperature, and V_m is the molar volume of the liquid at the vaporization temperature. The unit for the Hildebrand solubility parameter is $MPa^{0.5}$.

We predicted the miscibility of the API-polymer system using an empirical method for estimating miscibility based on differences between the API and polymer solubility parameters. If the $\Delta\delta_{API-polymer} < 7\ MPa^{0.5}$, the system is miscible; if $\Delta\delta_{API-polymer} > 10\ MPa^{0.5}$, the system is immiscible [38]. The physicochemical properties of TPZ were calculated using Eq. (4) [39] and Eq. (5) to predict the miscibility and glass transition temperature of the formulations. Crystallographic information on TPZ was obtained from the Cambridge Crystallographic Data Center (CCDC), with the deposition number 2142497.

$$V_m/nm^3 = \frac{V_{cell}/Å^3}{1{,}000Z} = \frac{V_{cell}/(cm^3 mol^{-1})}{602.2Z} \quad (4)$$

$$\rho = Z \times \frac{M}{N_A V_{cell}} \quad (5)$$

where Z represents the number of formula units in a crystallographic unit cell, V_{cell} is the crystal unit cell volume, the factor 602.2 [$=6.022\times10^{23}\ mol^{-1}/10^{21}\ nm\ cm^3$] converts cm^3/mol to nm^3 per formula unit using the Avogadro constant N_A, and ρ and M are the density and molar mass, respectively.

4. Physicochemical Characterization

The PXRD patterns were acquired using an XRD (Rigaku MiniFlex 600, Tokyo, Japan) with a Cu Kα radiation source (λ= 1.5406 Å) generated at 40 kV and 15 mA. PXRD measurements were conducted over a 2θ range of 4-40°, with a step size of 0.02° and a scan rate of 10°/min. The peak positions and areas were estimated using the instrument Guidance. MDSC analysis was performed using a DSC 2500 calorimeter (TA Instruments, New Castle, DE, USA). Each sample (5 mg) was encapsulated in an aluminum pan and scanned from 0 to 250 °C at a heating rate of 3 °C/min under a nitrogen atmosphere (N_2 flow rate: 50 mL/min). The modulation amplitude was maintained at ±1 °C for one min. The instrument was calibrated for heating data analysis against the melting properties of indium, and the heat capacity signal was calibrated using sapphire. TGA was conducted using an analyzer (Scinco N-1000, Seoul, Korea). Each powder sample (10 mg) was placed in a platinum pan and scanned from 30 °C to 800 °C at a heating rate of 5 °C/min under a nitrogen atmosphere (the same as in MDSC).

A Spectrum Two® attenuated total reflectance (ATR)-FTIR spectrometer (Perkin Elmer, Waltham, MA, USA) was used to acquire the IR spectra of various specimens in the solid state. Each spectrum was collected for a PASD powder specimen in the wavenumber range 4,000-450 cm^{-1} with a resolution of 4 cm^{-1}. ^{1}H SS-NMR measurements were obtained using a Bruker Advance Neo spectrometer (MA, USA) with a Larmor frequency of 600 MHz for ^{1}H nuclei. The magic-angle spinning (MAS) technique was used to improve sample resolution in the NMR spectra. A 1.9 mm triple CP/MAS probe and a 1.9 mm (O.D)-diameter zirconia rotor were used for all experiments. The spinning rate was 40 KHz and the 1H chemical shifts were referenced to adamantane at 1.85 ppm. For accelerated stability testing, the PASD powders were aged in a constant temperature and humidity chamber (Memmert HPP110eco, Schwabach, Germany) at 40 °C and 75% RH. The PASD samples were taken from the chamber every week to detect changes in the appearance and degree of crystallization during aging via PXRD measurements.

The *in vitro* dissolution test of the PASD solids was performed using the paddle method with a USP 2 dissolution apparatus (Dissolution tester 2100C; Distek, NJ, USA). A total of 400 mg of each powder sample (TPZ and three kinds of TPZ-PASD formulations) was added to 500 mL of a phosphate buffer solution (pH 6.8) with 50 rpm rotation at 37.0±1.0 °C. Excipients or surfactants were not used for the augmented dissolution test. The dissolution test was conducted by placing only each PASD powder in the buffer medium to prevent the force of compression from the pellet press from affecting PASD stability. Aliquots of 3 mL volumes were withdrawn at specific time intervals and filtered through a 0.45 μm syringe filter, followed by HPLC measurements. All PASD sample powders used for dissolution testing were gently ground for deagglomeration. To minimize the effect of particle size on the dissolution rate, each powder sample was sieved (mesh #120 and #230) to collect 63-125 μm particles. The TPZ concentration was determined using an HPLC system (Shimadzu UFLC, Kyoto, Japan) with a Zorbox SB-C18 column (4.6×250 mm, 5 μm; Agilent, Santa Clara, CA, USA) maintained at a temperature of 37.0±1.0 °C. The mobile phase comprised water with 0.1% (v/v) formic acid (A) and HPLC-grade methanol (B). Isocratic elution was performed using a water-methanol mixture (30 : 70). The flow rate was 1 mL/min, and the sample injection volume was 10 μL. Absorbance was measured at 262 nm to avoid interference with other compounds.

To analyze the *in vivo* absorption behavior, each formulation was orally administered to male Sprague-Dawley (SD) rats. All *in vivo* experiments were carried out by the Chaon Lab (Seongnam, Gyeonggi, Korea), an authorized non-clinical CRO. Blood was collected at designated intervals to evaluate *in vivo* absorption dynamics. The blood concentration of TPZ was analyzed using liquid chromatography-mass spectrometry (LC-MS/MS). Pharmacokinetic information, such as the area under the blood drug concentration-time curve (AUC), peak plasma concentration (C_{max}), time to peak plasma concentration (T_{max}), and half-life ($t_{1/2}$), were obtained from the TPZ concentration trend for each PASD. Three groups of rats (n=3 each) were used to evaluate the *in vivo* profile and were reared in a breeding room with environmental conditions of 23±3 °C, 50± 20% relative humidity, 10-15 ventilations/h, 12-h/12-h light/dark cycles, and 150-200 lx illumination. A prescribed dose of the drug was orally administered to the test animals. The test group fasted for more than 12 h, and all test groups were administered with a dose of 10 mL/kg. Blood was collected at the following intervals: 15 and 30 min; and 1, 3, 6, 12, and 24 h. The volume of blood col-

lected at each time point was 300 μL; the collected blood was placed in a heparin-treated (5 IU/mL) tube and mixed well before further analyses.

The TPZ concentration in the plasma was evaluated using an LC-MS/MS system (Agilent 1200 Series, Santa Clara, CA, USA) equipped with a Zorbox Eclipse C18 column (3.0×100 mm, 3.5; Agilent) at 30 °C. The mobile phase was composed of water containing 0.1% (v/v) formic acid in 10 mM ammonium formate buffer (A) and 0.1% (v/v) formic acid in HPLC-grade methanol/MeCN (1 : 1, v/v) (B). Isocratic elution was performed using a mixture of the mobile phases, A and B (30 : 70). The flow rate was 0.5 mL/min, the sample injection volume was 2 μL, and the sample temperature was 10 °C. The MS system used was an AB Sciex 4000 QTrap system (LC/MS, SCIEX, Framingham, MA, USA) equipped with an electrospray ionization source. The source-dependent parameters, such as curtain gas, collision gas, ion source gas 1 and gas 2, ion spray voltage, and ion source temperature, were optimized to 20 psi, 60 psi (gas 1 and gas 2), 5,300 V, and 450 °C, respectively. The analyte-dependent parameters for TPZ and its

Table 1. Predicted miscibility between TPZ and the three polymers

	δ (MPa$^{0.5}$)		$\Delta\delta$ (MPa$^{0.5}$)	Predicted miscibility
	API	Polymer	[δ_{TPZ}-$\delta_{polymer}$]	
TPZ	17.5[a]			
HPMCAS		23.6[b]	6.13	Miscible
Carbomer		23.0[c]	5.71	Miscible
PVP		24.3[d]	6.81	Miscible

[a] Calculated by Eq. (3)-(5); [b-d] Data from [40-42]

Table 2. Calculated glass transition temperatures of the three TPZ-containing PASD materials at 50% drug loading

	Density (ρ) (g/cm^3)		T_g for TPZ (°C)	T_g for polymer (°C)	Weight fraction (w_x)		$T_g^{m\text{-}calc}$ (Eq. (1) and (2)) (°C)
	API	Polymer			w_1	w_2	
TPZ	1.40[a]		102.0[a]		-	-	
TPZ-HPMCAS		1.28[b]		119.8[e]	0.5	0.5	111.1
TPZ-carbomer		1.40[c]		131.3[e]	0.5	0.5	116.1
TPZ-PVP		1.18[d]		178.8[e]	0.5	0.5	140.1

[a] Calculated by Eq. (4)-(5); [b-d] Data from [44-46], [e] Experimental data

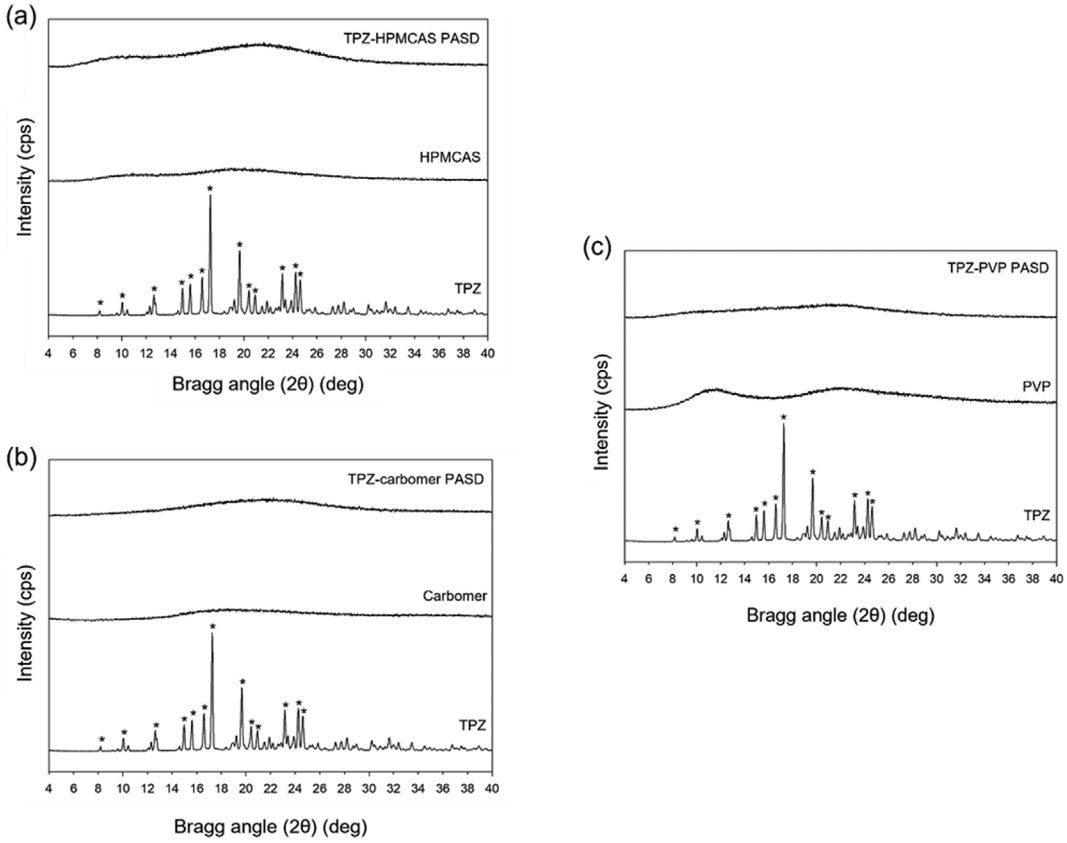

Fig. 1. PXRD patterns of (a) TPZ-HPMCAS, (b) TPZ-carbomer, and (c) TPZ-PVP PASD materials. * denote the main diffraction peaks of crystalline TPZ.

concentration were declustering potential (DP)=76 V and collision energy=21 V. The MRM used to evaluate TPZ was 388.2 m/z.

RESULTS AND DISCUSSION

1. Theoretical Calculation

Prior to PASD preparation, Eqs. (1)-(5) were utilized to predict the miscibility between TPZ and each polymer and estimate the glass transition temperature of the PASD materials. The solubility parameter difference approach [38] predicts that two components are miscible if their $\Delta\delta$ is less than 7 $MPa^{0.5}$. However, if their $\Delta\delta$ is more than 10 $MPa^{0.5}$, they are predicted to be immiscible. As shown in Table 1, all combinations of TPZ and each polymer (e.g., HPMCAS, carbomer, or PVP) are predicted to be miscible. Nevertheless, the carbomer showed greater miscibility with tegoprazan than did PVP.

The calculated glass transition temperatures ($T_g^{m\text{-}calc}$) of the three PASD solids are summarized in Table 2. As all three polymers have a T_g higher than TPZ, their incorporation as PASD materials is expected to increase their $T_g^{m\text{-}calc}$, thus enhancing the physical stability of TPZ. In this study, drug loading was fixed at 50% based on preliminary studies. In terms of $T_g^{m\text{-}calc}$ elevation, we anticipated that the TPZ-PVP materials would provide the best PASD system. However, if we compare the results from Tables 2 and 3, we notice that these two effects are conflicting. Therefore, lower drug loading might be one of the primary factors that could modify the thermodynamic nature and crystallization driving force of PASDs [43].

2. Characterization of PASD Powders

The PXRD patterns of all materials are shown in Fig. 1. The pure crystalline TPZ reveal sharp diffraction peaks at several Bragg angles (marked as *), whereas the three polymers do not show noticeable peaks alone. All PASD powders exhibit halo-shaped patterns typical of amorphized materials. Because the PXRD patterns of all TPZ-polymer physical mixtures (not shown) retained the peaks of crystalline TPZ, mechanical mixing using a milling apparatus was insufficient to amorphize TPZ.

The thermal characteristics of the PASD materials were determined using MDSC and TGA, and the results are shown in Figs. 2 and 3, respectively. The melting point of pure crystalline TPZ was measured as 223.5±1.3 °C, and the MDSC thermograms of the three polymers are illustrated in Fig. S2. As shown in Fig. 2, none of the PASD samples exhibits peaks other than the glass transition temperature ($T_g^{m\text{-}meas}$). For reference, observing the T_g of the PASD materials was extremely difficult using ordinary DSC. A distinctive single T_g for PASD materials comprising drugs and polymers with different T_g values has been widely considered a strong indication of ASD formation with good homogeneity [47]. Therefore, the PASD materials prepared were sufficiently good in terms of

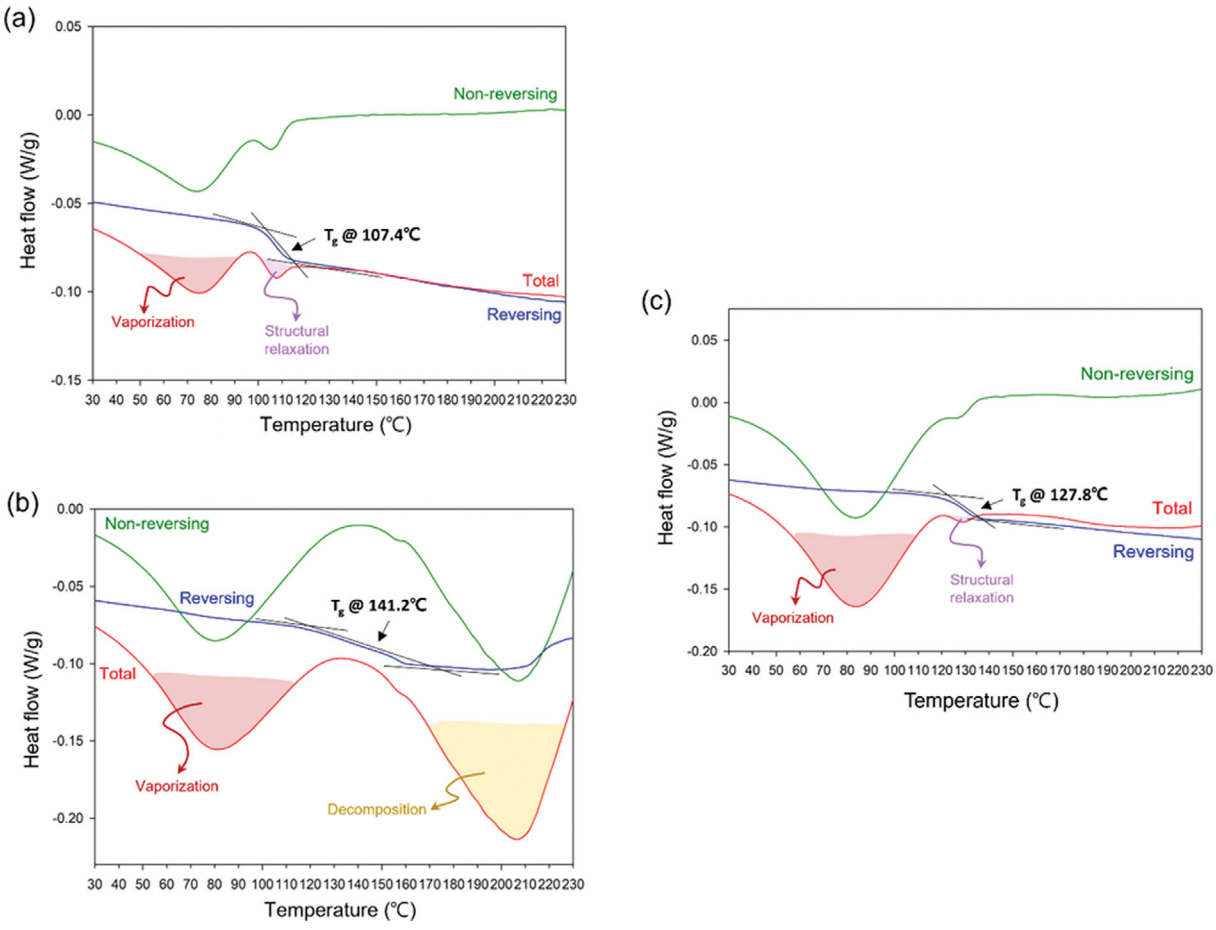

Fig. 2. Annotated MDSC thermograms of (a) TPZ-HPMCAS, (b) TPZ-carbomer, and (c) TPZ-PVP PASD materials.

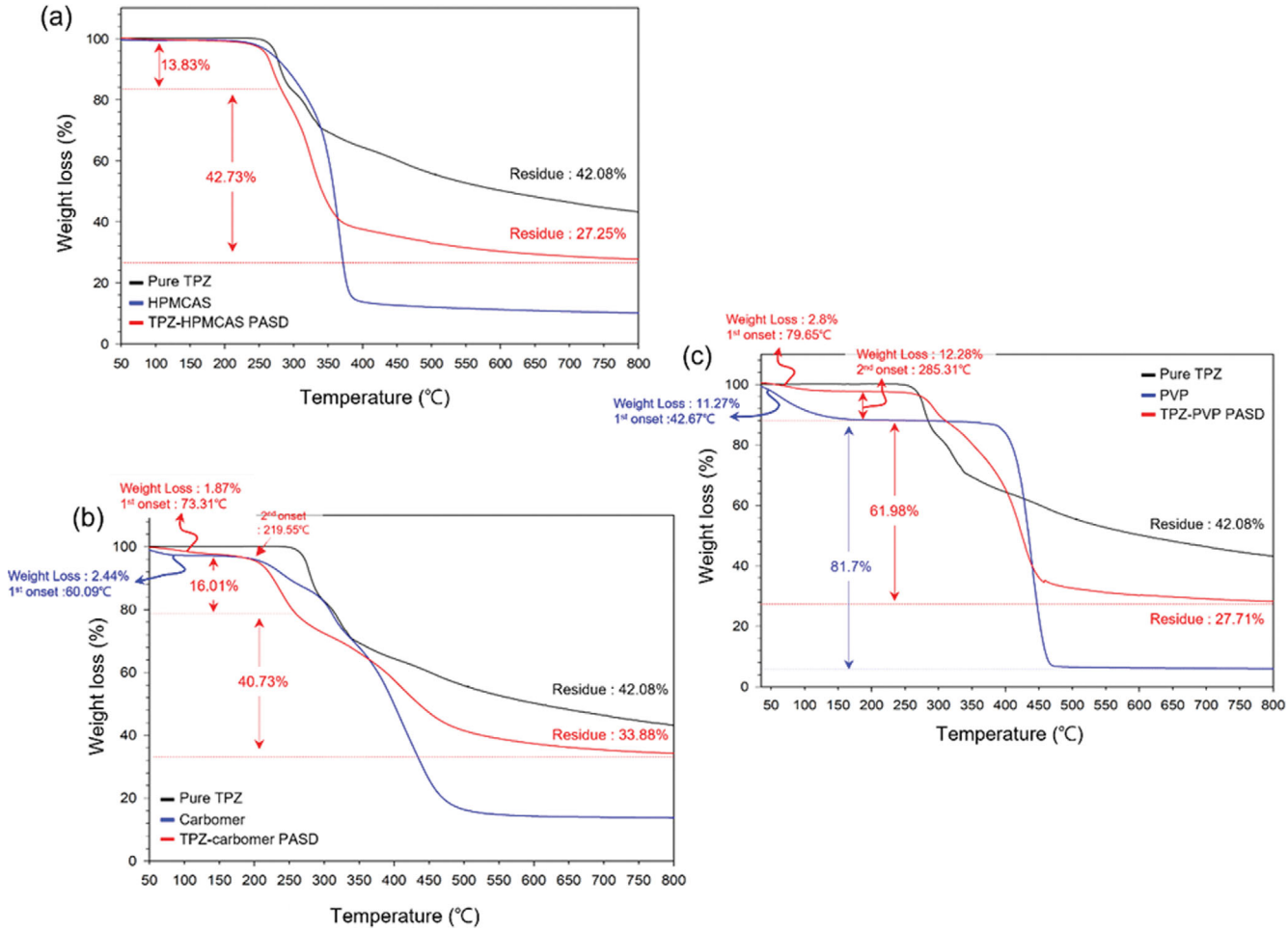

Fig. 3. Annotated TGA thermograms of (a) TPZ-HPMCAS, (b) TPZ-carbomer, and (c) TPZ-PVP PASD materials.

amorphization within polymer matrices.

As seen in Fig. 2(a), the TPZ-HPMCAS PASD shows a single $T_g^{m\text{-}meas}$ at 107.4 °C, which is similar to the theoretical value given in Table 2. With the "total heat flow" graph presented in Fig. 2, we could regard the endothermic peak due to melting at 107.4 °C. However, this is a structural relaxation phenomenon commonly observed at T_g, and there is no distinguishable signal change on the "reverse heat flow" graph. Therefore, the TPZ-HPMCAS PASD has a $T_g^{m\text{-}meas}$ of 107.4 °C. The broad endothermic peak observed at 75.2 °C is presumably attributed to the vaporization of residual solvent within the PASD or raw materials. This speculation can be proved through the weight loss observed in the TGA thermogram for TPZ-HPMCAS PASD at 77.3 °C (1st onset, Fig. S3), since a specific signal is not observed in the reverse heat flow plot in Fig. 2(a).

The TPZ-carbomer PASD also shows a single $T_g^{m\text{-}meas}$ at 141.2 °C (Fig. 2(b)). Generally, when a low T_g compound is mixed with a higher T_g compound, the T_g corresponding to the mixture falls somewhere between two T_g values [48]. However, the $T_g^{m\text{-}meas}$ of the TPZ-carbomer PASD is remarkably higher than the T_g of either material (T_g of TPZ and carbomer: 102.0 °C and 133.1 °C, respectively). Considering that a detectable amount (~2 wt%) of residual methanol in this PASD would have lowered the true T_g value, an increase of ~25 °C in the T_g of the TPZ-carbomer PASD formulation is remarkable. From this, it is concluded that the TPZ-carbomer PASD was not produced from the spatial dispersion of TPZ molecules in the carbomer matrix. Instead, it was formed from stronger intermolecular interactions, such as hydrogen bonding, between the TPZ and carbomer chains. One thing to note in Fig. 2(b) is the huge endothermic peak at 208 °C annotated as "decomposition," which is supported by the second onset of the TGA thermogram at 219.6 °C (Fig. 3(b)). The decomposition temperature for the PASDs with the other two polymers appears to be substantially higher than 250 °C.

A single T_g was observed at 127.8 °C for the TPZ-PVP PASD formulation. However, in this case, the measured $T_g^{m\text{-}meas}$ was substantially lower than $T_g^{m\text{-}calc}$ shown in Table 1. The overall shape of the MDSC thermograms of TPZ-PVP PASD is very similar to that of TPZ-HPMCAS, except for the size of the endothermic vaporization peak. This peak size is well-matched to the large decrease due to weight loss in the TGA thermogram of TPZ-PVP PASD, as shown in Fig. 3(c). In summary, a single T_g was observed for all PASDs of TPZ, which partly proves that a good ASD could be prepared for TPZ using the three polymers. When carbomer was used as the polymer matrix, stronger intermolecular interactions increased the $T_g^{m\text{-}meas}$ value.

FT-IR spectroscopy is widely used to examine the physicochem-

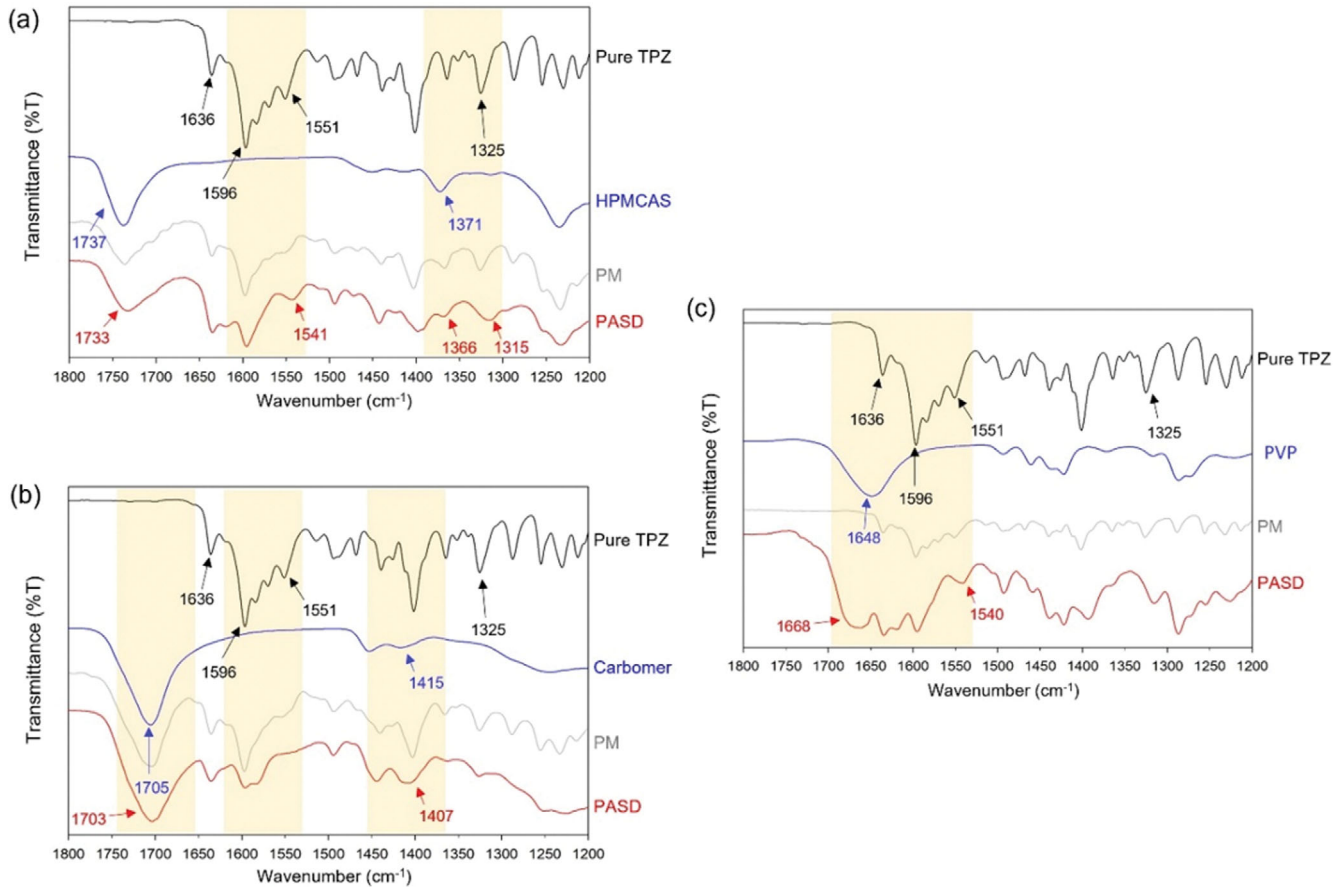

Fig. 4. IR spectra of (a) TPZ-HPMCAS, (b) TPZ-carbomer, (c) TPZ-PVP PASD materials: 1,800-1,200 cm^{-1} region for O-H.

ical characteristics of PASD materials [27,46,49]. Fig. 4 and Fig. S4 show the IR spectra of the three PASD powders, each divided into two wavenumber ranges (1,800-1,200 cm^{-1} and 3,600-2,500 cm^{-1}) for a better comparison. Overall, the IR spectrum of each physical mixture of TPZ and polymer appears to be a combination of two components, whereas that of each PASD material shows clear differences in several absorption peaks. Accordingly, our discussion on the IR spectra is concentrated on the yellow-colored regions, where the differences in the IR spectra between materials are more apparent.

The functional groups of the relevant hydrogen bonds of the polymer are listed in Table 3 [50]. All polymers have an acceptor functional group for hydrogen bonding in either the ether or acyl groups. However, one difference is that both HPMCAS and carbomer have a donor functional group (e.g., carboxylic acid or alcohol) for hydrogen bonding, while PVP does not. Hydrogen bonding interactions between two or more compounds tend to affect the IR spectra via frequency shifts or increases in the peak intensity for the bands of functional groups directly involved in the H-bonded bridges [51]. Hence, differences in intermolecular interactions between TPZ and polymers are expected when forming PASDs with functional groups that act as acceptors.

As shown in Fig. 4(a), in the case of HPMCAS [19,52,53], two absorption peaks are related to the carbonyl group moiety at 1,737 cm^{-1} and O-H bending at 1,371 cm^{-1}. As for TPZ, IR absorption peaks are observed at 1,636, 1,596, 1,551, and 1,300 cm^{-1} for C=O stretching, C=N stretching, N-H in-plane bending, and C-N stretching, respectively [54-56]. The spectrum of TPZ-HMPCAS is mostly attenuated. For the TPZ-HPMCAS PASD, the two peaks for the N-H bending and C-N stretching of TPZ shift from 1,551 cm^{-1} to 1,541 cm^{-1} and from 1,325 cm^{-1} to 1,315 cm^{-1}, respectively. These results are worth noting because hydrogen bonding causes a red shift in the IR spectrum. Moreover, the peaks at 1,737 and 1,371 cm^{-1} for HPMCAS are red-shifted to 1,733 and 1,366 cm^{-1}, respectively, after PASD formation with TPZ. Presumably, the acidic carbonyl group of neat HPMCAS forms hydrogen bonds with TPZ, so peak boarding and shift occur, similar to previous studies [57,58].

On the other hand, as they were physically mixed, many peaks for neat HPMCAS or pure TPZ vanished in the 3,500-2,500 cm^{-1} wavenumber range (Fig. S4(a)). In addition, IR peaks related to the C-H stretching of HPMCAS are partially observed, whereas peaks for TPZ disappear completely or merge in the 3,400-3,000 cm^{-1} range. These outcomes are supposedly caused by hydrogen bonding between TPZ and HPMCAS, which is observed to be much stronger for PASD materials than for physical mixtures. In the TPZ-carbomer pair, the carbomer presents absorption peaks at 1,705 and 1,415 cm^{-1}, corresponding to C=O stretching and O-H bending, respectively (Fig. 4(b)) [59]. In this spectrum, the two peaks associated with -R(CO)-OH in the carbomer red-shift and broaden, owing to hydrogen bonding between TPZ and the car-

Table 3. Characteristics of polymers relevant for hydrogen bonding

Polymer	Functional group	pKa	H-Donor?	Donor strength	Acceptor?	Acceptor strength
Carbomer	R-C(O)-OH	4.5	Yes	Very strong	Yes	Medium
HPMCAS	R-O-R	-	No	-	Yes	Medium
	R-C(O)-O-R	-	No	-	Yes	Medium
	R-OH	-	No	Strong	Yes	Medium
	R-C(O)-OH	4.5-5	Yes	Strong	Yes	Medium
PVP	R-C(O)-N-R_2	-	No	-	Yes	Very strong

Table 4. Summary of IR spectrum data and their corresponding marker bands

	IR marker bands (cm^{-1})	Assignment[a]
TPZ	1,636	νC=O
	1,596	νC=N
	1,551	ρN-H
	1,325	νC-N
HPMCAS	3,471	νO-H, non-hydrogen bonding in HPMCAS
	1,737	νC=O
	1,371	ρO-H
Carbomer	1,705	νC=O
	1,415	νC-O coupled with ρO-H
PVP	1,648	νC=O, non H-bonded
TPZ-HPMCAS	1,733	Shifted νC=O peak of HPMCAS, when H-bonded to TPZ
	1,541	Shifted νN-H peak of TPZ, when H-bonded to HPMCAS
	1,366	Shifted ρO-H peak of HPMCAS, when H-bonded to TPZ
	1,315	Shifted νC-N peak of TPZ, when H-bonded to HPMCAS
TPZ-carbomer	1,703	νC=O for carbomer
	1,407	Shifted ρO-H peak of carbomer, when H-bonded to TPZ
TPZ-PVP	1,668	Shifted νC=O peak of PVP, when H-bonded to TPZ
	1,540	Shifted νN-H peak of TPZ, when H-bonded to PVP

[a] Data from [61-63]

bomer. In addition, several absorption peaks for the physical mixture disappear from the spectrum of the PASD formulation. Significant changes are also observed in the 3,600-2,500 cm^{-1} range, as shown in Fig. S4(b). The absorption peaks observed in the spectra of TPZ and its physical mixture mostly broaden or disappear because of the strong hydrogen bonding between TPA and the carbomer.

The IR spectrum of TPZ-PVP PASD (Fig. 4(c)) shows a "blue shift" from 1,648 cm^{-1} to 1,668 cm^{-1}. The peak at 1,600 cm^{-1} is assigned to the C=O stretching of PVP [19]. Since the carbonyl group in PVP is presumed to form an H-bond with the N-H in TPZ, a shift of 19 cm^{-1} is observed relative to the non-hydrogen bonded carbonyl in PVP at 1,648 cm^{-1} [60]. Moreover, the peak centered at 1,551 cm^{-1}, which is associated with the C-N-H of imidazole in TPZ, shifts to 1,540 cm^{-1}. Nonetheless, the IR spectra of the TPZ-PVP PASD are very similar to those of the physical mixtures, although little change is observed in the 1,800-1,200 cm^{-1} region. Our observations and interpretations of the FT-IR spectra are summarized in Tables 3 and 4.

^{1}H SS-NMR analysis was also performed to investigate the intermolecular interactions caused by the amorphization of TPZ with the polymers. The 1H CP-MAS NMR spectra of TPZ, polymers, and the resulting PASD materials are shown in Fig. 5. Differences in the chemical shifts of the PASDs with respect to the individual materials are clearly observed. Generally, ^{1}H chemical shifts of O···H···N-type hydrogen bonds are observed in the range of 9-18 ppm [64]. Therefore, the single 1H peak at 13.7 ppm in the TPZ spectrum is associated with the presence of an intramolecular N-H···O=C hydrogen bond typical of TPZ in its crystal form. HPMCAS gives rise to a relatively broad 1H NMR spectrum that spans a frequency range of 0-8 ppm because it possesses numerous alkyl protons and hydroxyl protons (Fig. 5(a)). HPMCAS has no aromatic protons; thus, the small shoulder peak at 7.3 ppm would likely be assigned to the hydroxyl protons. TPZ-HPMCAS PASD displays two 1H peaks at approximately 3.1 and 6.5 ppm, corresponding to aliphatic and aromatic protons, respectively (Fig. 5(a)).

Interestingly, two new proton resonances are observed at 15.1 and 12.3 ppm, which could be assigned to the O-H···N and N-H···O hydrogen bonds, respectively. Based on the FT-IR results, the formation of the TPZ-HPMCAS PASD involves proton transfer from

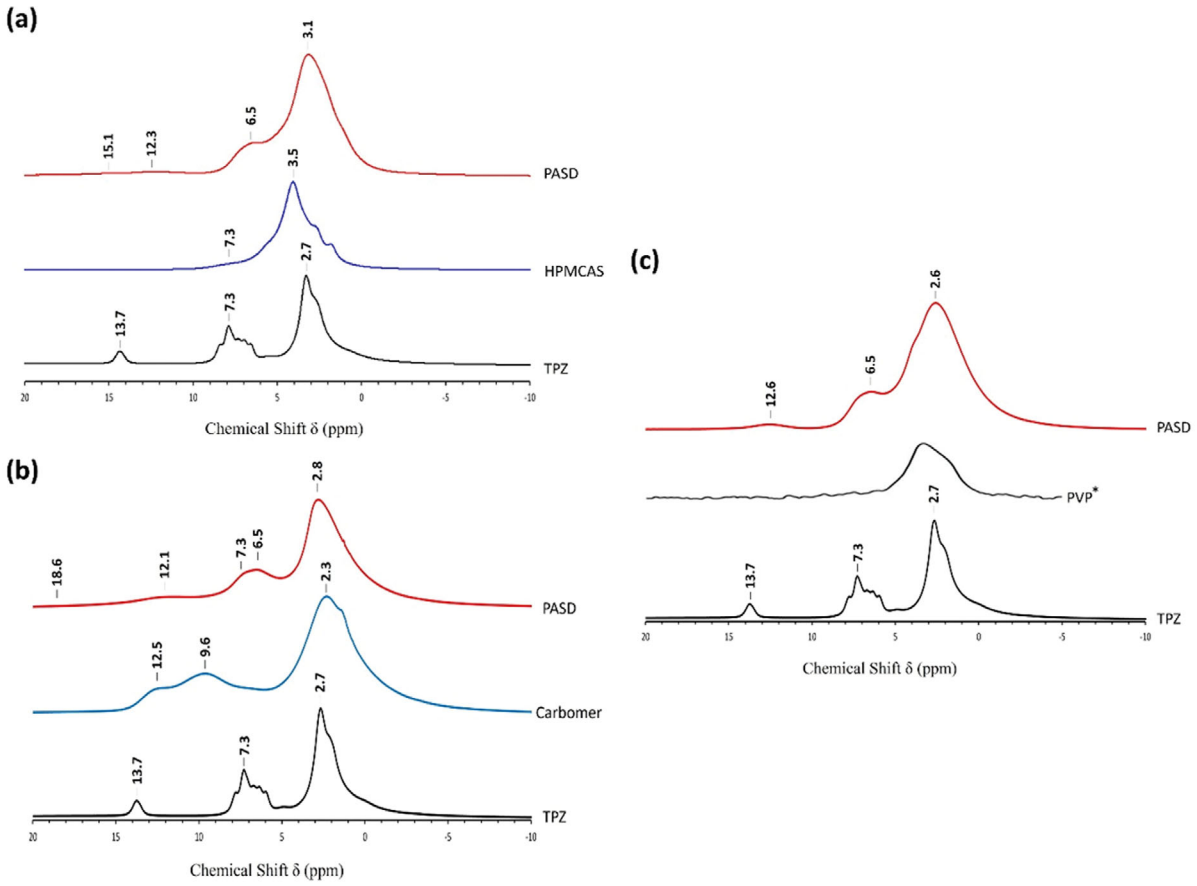

Fig. 5. ^{1}H SS-NMR spectra of (a) TPZ-HPMCAS, (b) TPZ-carbomer, and (c) TPZ-PVP PASD materials; The ^{1}H SS-NMR spectrum of PVP was adopted from [65].

the -COOH of the polymer to the N=C of TPZ. Therefore, the former signal moves from 7.3 ppm in HPMCAS to 15.1 ppm in the PASD, indicating the presence of a strong hydrogen bond. In contrast, the small 1H peak shifts from 13.7 in TPZ to 12.3 in the PASD, which means that the hydrogen bond coordination involving the N-H of TPZ is changed upon PASD formation. This suggests that the formation of TPZ-HPMCAS interactions disrupts the intermolecular TPZ-TPZ interactions [57].

The ^{1}H NMR spectrum of the carbomer is characterized by resonances at 9.6 and 12.5 ppm, as shown in Fig. 5(b). These peaks could be attributed to the carboxylic proton, which were observed at a magnetic field lower than 10 ppm [66,67]. The two 1H signals originating from the -OH group of the carboxylic acid are likely to be associated with the strength of hydrogen bonds formed by interacting carboxylic acid dimers, that is, O-H···O=C or O-H···O-H. Thus, the -COOH of the carbomer is likely to form a hydrogen bond with the imidazole N of TPZ in the TPZ-carbomer PASD. The presence of a strong O-H···N hydrogen bond in the TPZ-carbomer PASD is confirmed by the 1H MAS spectrum, which is characterized by a peak at 18.6 ppm (Fig. 5(b)).

Indeed, the high-frequency shift of the hydrogen-bonded atom (from 9.6 and 12.5 to 18.6 ppm) is directly related to the presence and the strength of the hydrogen bond [68]. Similar to the TPZ-HPMCAS PASD, an up-field shift from 13.7 ppm in TPZ to 12.1 ppm in the TPZ-carbomer PASD is also observed, suggesting the good dispersion of TPZ in the carbomer matrix. It is well known that a larger chemical shift results in stronger hydrogen bonds. The TPZ-carbomer and TPZ-HPMCAS PASDs formed molecular interactions with the imidazole ring of TPZ through the carboxylic acid of each polymer, while 1H chemical shifts for the O-H of the PASDs are found at 18.6 and 15.1 ppm. Therefore, the molecular interactions in the TPZ-carbomer PASD were stronger than those in the TPZ-HPMCAS PASD, possibly because a larger proportion of TPZ molecules in the TPZ-carbomer PASD formed TPZ-polymer interactions compared to those in TPZ-HPMCAS PASD [57].

This finding could explain why the T_g of the TPZ-carbomer PASD is higher than that of the carbomer. Furthermore, the formation of strong COOH-N=C interactions in the dispersion of TPZ with the carbomer and HPMCAS has led to the excellent physical stability of the PASD systems. For the TPZ-PVP PASD, one 1H peak (12.6 ppm) was observed at a magnetic field lower than 10 ppm, indicating the formation of TPZ–PVP interactions involving the N-H group of TPZ. This signal moved from 13.7 ppm in TPZ to 12.6 ppm in the PASD, indicating a weaker interaction in the PASD than in TPZ alone. This shift was also observed in the two PASD systems, whereas there were no supplementary interactions in the TPZ-PVP PASD. Therefore, the physical stability of the TPZ-

HPMCAS and TPZ-carbomer PASD formulations should be expected to be better than that of the TPZ-PVP material.

In summary, the implications of the SS-NMR results are in good agreement with those from the FT-IR analysis; that is, there is a stronger hydrogen bonding propensity from the two anionic polymers than from the non-ionic polymer PVP. It was previously reported that the carbomer resulted in salt formation when amorphizing basic drugs with a ΔpK_a>4 [23]. In our case, however, the ΔpK_a was <1; hence, salt formation did not occur. Accordingly, the intermolecular interactions between TPZ and the two ionic polymers were governed by the strength of hydrogen bonding.

3. Stability Test

All PASD powders were stored in a temperature-humidity chamber set at 40 °C and 75% RH until they were evaluated to determine whether crystallization occurred after one and three months under accelerated storage stability conditions. All formulations were evaluated using the naked eye, PXRD, and PLM (Fig. S5). The PXRD patterns are shown in Fig. 6. As mentioned, all PASDs were fully prepared in an amorphous state. Two PASD powders, TPZ-HPMCAS and TPZ-carbomer, retained their amorphous state after three months of storage, while the TPZ-PVP PASD showed apparent crystallization of TPZ. The above results indicate the absence and/or inadequacy of hydrogen bonding between TPZ and PVP, as inferred from other analyses, such as SS-NMR or FT-IR.

Moreover, it was previously reported that the crystallization of dispersed drugs within PVP occurs under accelerated stability testing conditions because strong interactions (e.g., hydrogen bonding or ionic bonding) are not formed between PVP and weakly basic drugs [12,20]. Theoretically, if the T_g of a polymer is higher than a drug and it is mixed well with a drug at the molecular level, the T_g of the PASD would increase; accordingly, its stability will be enhanced [69]. Although the T_g of PVP was the highest and the T_g of the TPZ-PVP PASD was not the lowest among the three polymers, the amorphization of TPZ with PVP resulted in the lowest physical stability among the three polymers. Additionally, birefringence images (Fig. S5) for the crystals were not detected via PLM measurements on the TPZ-HPMCAS and TPZ-carbomer PASD powders. As a result, the stability of a PASD material might not be strongly dependent on its absolute T_g value, but could be significantly affected by the extent of intermolecular interactions, such as hydrogen bonding within amorphized structures. This is in contrast with the findings reported in other studies [20,53,70].

4. *In Vitro* Dissolution and *In Vivo* Absorption Study

Since the stability of the TPZ-PVP PASD formulation was far below our expectation, we performed *in vitro* dissolution and in vivo absorption measurements only for the other two PASD materials, using pure crystalline TPZ as the control. The drug dissolution profiles of the three materials are compared in Fig. 7(a). The two TPZ PASDs show substantially improved dissolution rates in an aqueous solution at pH 6.8. At pH 6.8, the TPZ-HPMCAS and TPZ-carbomer PASD powders rapidly dissolved within the first 5 min; thus, the drug concentrations were much greater than the

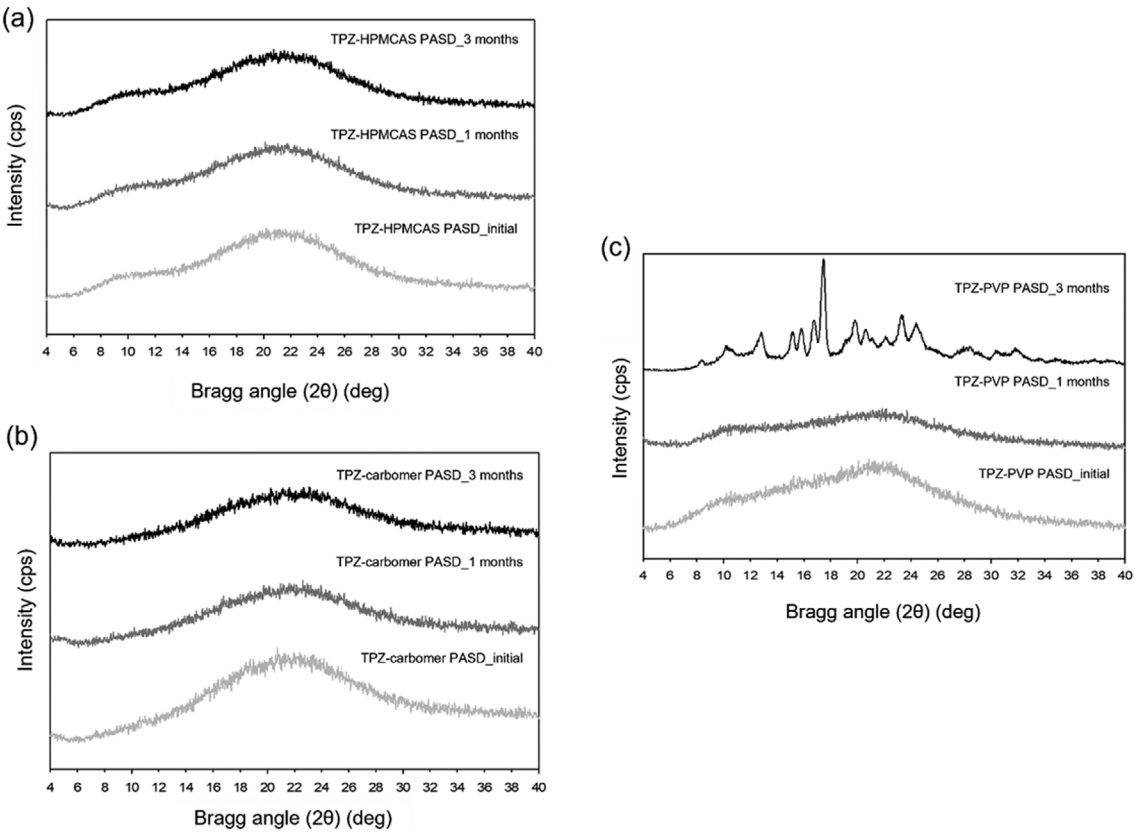

Fig. 6. PXRD patterns of (a) TPZ-HPMCAS, (b) TPZ-carbomer, and (c) TPZ-PVP PASD materials after storage for one month or three months at 40 °C and 75% RH.

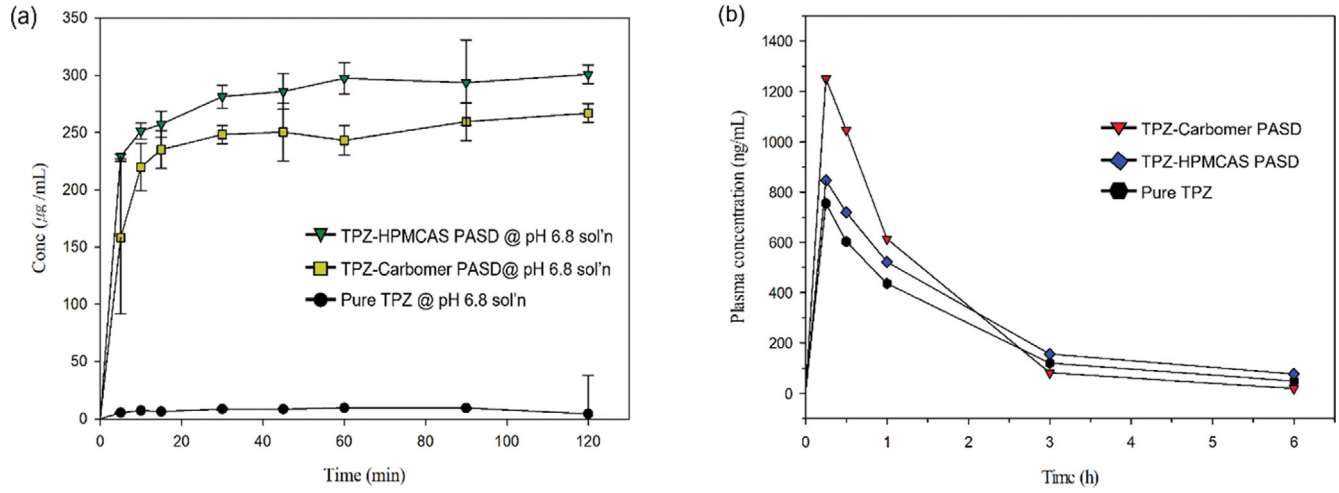

Fig. 7. Comparison of (a) *in vitro* powder dissolution and (b) *in vivo* drug absorption profiles of the TPZ-HPMCAS and TPZ-carbomer PASD materials with crystalline TPZ.

concentration of pure TPZ. After 40 min, the drug concentrations reached saturation levels; the maximum concentrations of the TPZ-HPMCAS and TPZ-carbomer PASDs were 297.6±0.5 and 250.32±1.4 μg/mL, respectively. In comparison, the maximum concentration of pure TPZ was 10.96±4.0 μg/mL. HPMCAS and carbomer are both pH-responsive and pH-dependent polymers [71-74]. At pH 6.8, HPMCAS was presumed to increase drug release in PASD systems [72,73]. In contrast, a conformational transition from the swollen state to drug release occurred in the PASD materials composed of carbomer chains [71,74]. The difference in drug dissolution mechanism might be associated with the *in vivo* absorption behavior of a drug [75].

The *in vivo* drug absorption profiles of the two PASD materials and pure TPZ are compared in Fig. 7(b), and the estimated pharmacokinetic parameters are summarized in Table 5. The two PASD materials show better drug absorption than TPZ alone. The *in vivo* C_{max} of the TPZ-carbomer PASD is 50% higher (1,250.23±647.29 ng/mL) than that of the TPZ-HPMCAS pair (846.95±307.58 ng/mL) and crystalline TPZ (755.65±247.91 ng/mL) at 15 min. After the t_{max}, the drug concentrations decrease rapidly, especially for the TPZ-carbomer pair. Owing to the rapid decrease in drug concentration, the AUC_{last} values of the two PASD powders are slightly (~25%) greater than that of pure TPZ. Nevertheless, the standard deviation in C_{max} and AUC_{last} values is always considerable as shown in Table 5.

One of the primary reasons for the rather disappointing *in vivo* enhancement could be the pH dependence of the two polymers, HPMCAS and carbomer. In particular, HPMCAS has poor solubility under acidic conditions (pH<2) [67-70]. In addition, it is reported that the pH conditions in SD rats are substantially different from those in humans [76,77]. The pH level of the rat intestine was lower than 6.8, the standard pH value used in *in vitro* dissolution studies. Hence, the dissolution of the two PASD materials should be reduced in the GI tract of rats. In this regard, rats might not be a suitable model for studying pH-sensitive PASD materials simulating human gastrointestinal tract conditions. In addition, a recent study showed that the above pH discrepancy issue was alleviated by employing a FaSSIF solution [76].

Table 5. Pharmacokinetics parameters of pure TPZ and two PASD formulations

	AUC_{last} [h*ng/mL]	C_{max} [ng/mL]	t_{max} [h]
TPZ	1,502.28±464.28	755.65±247.91	0.25
TPZ-HPMCAS	1,882.75±842.73	846.95±307.58	0.25
TPZ-carbomer	1,779.99±807.69	1,250.23±647.29	0.25

Another possible reason could be the rapid precipitation/crystallization of dissolved TPZ in the blood of the SD rats. The C_{max} *in vitro* reached 300 μg/mL quickly and was sustained up to 2 h as shown in Fig. 7(a), whereas C_{max} *in vivo* started to drop at a much lower concentration, as shown in Fig. 7(b), for the two PASD materials. In the bodies of SD rats, a large proportion of the dissolved TPZ from PASDs in a supersaturated state might have precipitated into solid particles. Nevertheless, this was not analyzed in this study. Additional *in vivo* tests with modified conditions and analytical studies of the precipitates are necessary to elucidate this.

CONCLUSIONS

We successfully developed polymer-based amorphous solid dispersion (PASD) materials with HPMCAS and carbomer for the insoluble drug tegoprazan (TPZ), which was approved in 2019 to treat gastroesophageal reflux disease. TPZ PASD powders were prepared using these two ionic polymers and a neutral polymer, PVP, and compared using theoretical and experimental tools. The miscibility and T_g of the PASD materials were calculated using the Hansen solubility parameter and the Gordon-Taylor equation. The formulations were characterized via in vitro dissolution and in vivo absorption tests, including several analytical techniques, such as PXRD, MDSC, TGA, FT-IR, ^{1}H SS-NMR, and accelerated stability tests.

The single T_g value for all PASD powders indicates that good amorphization of TPZ was achieved using the evaporation method.

The $T_g^{m\text{-}meas}$ for the TPZ-carbomer pair was higher than the predicted value, whereas it was lower for TPZ-PVP PASD. Molecular interactions were examined using FT-IR and ^{1}H SS-NMR measurements, which similarly indicated a significant difference in the extent of hydrogen bonding between three PASD materials. Consequently, the two PASD materials were clearly differentiated through accelerated stability testing. The TPZ-HPMCAS and TPZ-carbomer PASD powders showed no signs of crystallization, even after three months of aging at 40 °C/75% RH.

In vitro dissolution and *in vivo* absorption studies were performed on two stable PASDs and pure TPZ. The PASD powder exhibited remarkably higher *in vitro* dissolution rates than the crystalline TPZ powder. Although the PASD powders performed better than pure TPZ during *in vivo* absorption testing, the difference was smaller than what we expected based on *in vitro* dissolution results. The intermolecular hydrogen bonding plays a key role in determining the stability and dissolution behavior of PASD formulation when salt formation does not occur.

ACKNOWLEDGEMENTS

This research was financially supported by the Basic Science Research Program through the National Research Foundation of Korea (NRF-2020R1F1A106966813). This study was also supported by the Soonchunhyang University Research Fund.

NOMENCLATURE

ASD	: amorphous solid dispersions
ATR	: attenuated total reflectance
AUC	: area under curve
BCS	: biopharmaceutical classification system
CCDC	: cambridge crystallographic data center
DSC	: differential scanning calorimetry
FT-IR	: Fourier transform-infrared
GERD	: gastroesophageal reflux disease
HPMCAS	: hydroxypropyl methylcellulose acetate succinate
MDSC	: modulated differential scanning calorimetry
PAA	: polyacrylic acid
PASD	: polymer-based amorphous solid dispersion
PDF	: pair distribution function
PPI	: proton pump inhibitors
PVP	: polyvinylpirrolidone
PXRD	: powder x-ray diffraction
SS-NMR	: solid-state nuclear magnetic resonance
TDA	: total diffraction analysis
TGA	: thermogravimetric analysis
T_g	: glass transition temperature
$T_g^{m\text{-}calc}$	: calculated glass transition temperature of ASD
$T_g^{m\text{-}meas}$	: measured glass transition temperature of ASD
TPZ	: tegoprazan

SUPPORTING INFORMATION

Additional information as noted in the text. This information is available via the Internet at http://www.springer.com/chemistry/journal/11814.

REFERENCES

1. W. L. Chiou and S. Riegelman, *J. Pharm. Sci.*, **60**, 1281 (1971).
2. S. V. Bhujbal, B. Mitra, U. Jain, Y. Gong, A. Agrawal, S. Karki, L. S. Taylor, S. Kumar and Q. Zhou, *Acta Pharm. Sin. B.*, **11**, 2505 (2021).
3. R. Iyer, V. P. Jovanovska, K. Berginc, M. Jaklič, F. Fabiani, C. Harlacher, T. Huzjak and M. V. Sanchez-Felix, *Pharmaceutics*, **13**, 1682 (2021).
4. P. Pandi, R. Bulusu, N. Kommineni, W. Khan and M. Singh, *Int. J. Pharm.*, **586**, 119560 (2020).
5. D. M. Walden, Y. Bundey, A. Jagarapu, V. Antontsev, K. Chakravarty and J. Varshney, *Molecules*, **26**, 182 (2021).
6. J. Liu, H. Grohganz, K. Löbmann, T. Rades and N. J. Hempel, *Pharmaceutics*, **13**, 389 (2021).
7. C. G. Bavnhøj, M. M. Knopp, C. M. Madsen and K. Löbmann, *Int. J. Pharm. X*, **1**, 100008 (2019).
8. N. J. Hempel, K. Brede, N. E. Olesen, N. Genina, M. M. Knopp and K. Löbmann, *Int. J. Pharm.*, **544**, 153 (2018).
9. E. O. Kissi, M. T. Ruggiero, N. J. Hempel, Z. Song, H. Grohganz, T. Rades and K. Löbmann, *Phys. Chem. Chem. Phys.*, **21**, 19686 (2019).
10. H. Grohganz, P. A. Priemel, K. Löbmann, L. H. Nielsen, R. Laitinen, A. Mullertz, G. V. D. Mooter and T. Rades, *Expert Opin. Drug Deliv.*, **11**, 977 (2014).
11. N. K. Duggirala, J. Li, N. S. K. Kumar, T. Gopinath and R. A. Suryanarayanan, *ChemComm.*, **55**, 5551 (2019).
12. P. Mistry, S. Mohapatra, T. Gopinath, F. G. Vogt and R. Suryanarayanan, *Mol. Pharm.*, **12**, 3339 (2015).
13. H. Nie, Y. Su, M. Zhang, Y. Song, A. Leone, L. S. Taylor, P. J. Marsac, T. Li and S. R. Byrn, *Mol. Pharm.*, **13**, 3964 (2016).
14. S. Bandari, S. Jadav, B. B. Eedara, R. Jukanti and P. R. Veerareddy, *Korean J. Chem. Eng.*, **30**, 238 (2013).
15. K. Yuvaraja, S. K. Das and J. Khanam, *Korean J. Chem. Eng.*, **32**, 132 (2015).
16. H. Rostamian, M. N. Lotfollahi and A. Mohammadi, *Korean J. Chem. Eng.*, **37**, 2295 (2020).
17. K. Kothari, V. Ragoonanan and R. Suryanarayanan, *Mol. Pharm.*, **12**, 162 (2015).
18. T. Miyazaki, S. Yoshioka, Y. Aso and S. Kojima, *J. Pharm. Sci.*, **93**, 2710 (2004).
19. A. C. Rumondor and L. S. Taylor, *Mol. Pharm.*, **7**, 477 (2010).
20. D. Yu, J. Li, H. Wang, H. Pan, T. Li, T. Bu, W. Zhou and X. Zhang, *Eur. J. Pharm. Sci.*, **169**, 106086 (2022).
21. N. G. Solanki, K. Lam, M. Tahsin, S. G. Gumaste, A. V. Shah and A. T. M. Serajuddin, *J. Pharm. Sci.*, **108**, 1453 (2019).
22. S. Wang, C. Liu, Y. Chen, A. Zhu and F. Qian, *Mol. Pharm.*, **15**, 4643 (2018).
23. X. Yao, A. L. Neusaenger and L. Yu, *Pharmaceutics*, **13**, 1271 (2021).
24. X. Liu, X. Feng, R. O. Williams and F. Zhang, *J. Pharm. Investig.*, **48**, 19 (2018).
25. S. A. Raina, D. E. Alonzo, G. G. Z. Zhang, Y. Gao and L. S. Taylor, *Mol. Pharm.*, **11**, 3565 (2014).
26. Y. Song, X. Yang, X. Chen, H. Nie, S. Byrn and J. W. Lubach, *Mol. Pharm.*, **12**, 857 (2015).
27. M. S'ari, H. Blade, S. Cosgrove, R. Drummond-Brydson, N. Hon-

dow, L. P. Hughes and A. Brown, *Mol. Pharm.*, **18**, 1905 (2021).
28. H. Mori and H. Suzuki, *J. Neurogastroenterol. Motil.*, **25**, 6 (2019).
29. S. Han, H. Y. Choi, Y. H. Kim, J. Y. Nam, B. Kim, G. S. Song, H. S. Lim and K. S. Bae, *Aliment Pharmacol. Ther.*, **50**, 751 (2019).
30. N. Takahashi and Y. Take, *J. Pharmacol. Exp. Ther.*, **364**, 275 (2018).
31. J. G. Hwang, H. Yoo, J. W. Lee, G. S. Song, S. Lee and M. G. Kim, *Transl. Clin. Pharmacol.*, **27**, 80 (2019).
32. J. Ghim, M. C. Chin, J. Jung, J. Lee, S. Kim, B. Kim, G. S. Song, Y.-K. Choi and J.-G. Shin, *J. Clin. Pharmacol.*, **61**, 913 (2020).
33. Y. J. Kim, E. S. Kim, J. Y. Lee, H. W. Lee, J. H. Kweon, S. A. Lee, K. D. Choi, D. H. Ko and S. P. Heo, Korea Patent, KR101684053 B1 (2016).
34. E. S. Kim, M. K. Lee, S. A. Lee, K. D. Choi, J. S. Kim and H. C. Yoo, Korea Patent, KR101829706 B1 (2018).
35. D. T. Friensen, R. Shanker, M. Crew, D. T. Smithey, W. J. Curatolo and J. A. S. Nightingale, *Mol. Pharm.*, **5**, 1003 (2008).
36. M. Gordon and J. S. Taylor, *J. Appl. Chem.*, **2**, 493 (1952).
37. B. C. Hancock, P. York and R. C. Rowe, *Int. J. Pharm.*, **148**, 1 (1997).
38. D. J. Greenhalgh, A. C. Williams, P. Timmins and P. York, *J. Pharm. Sci.*, **88**, 1182 (1999).
39. L. Glasser, *J. Chem. Educ.*, **88**, 581 (2011).
40. S. Jankovic, G. Tsakiridou, F. Ditzinger, N. J. Koehl, D. J. Price, A. R. Ilie, L. Kalantzi, K. Kimpe, R. Holm, A. Nair, B. Griffin, C. Saal and M. Kuentz, *J. Pharm. Pharmacol.*, **71**, 441 (2019).
41. T. Nakano, N. Saito and H. Minami, *Langmuir*, **36**, 11957 (2020).
42. L. Li, Z. Jiang, J. Xu and T. Fang, *J. Appl. Polym. Sci.*, **131**, 40304 (2014).
43. F. Qian, J. Huang and M. A. Hussain, *J. Pharm. Sci.*, **99**, 2941 (2010).
44. K. Lehmkemper, S. O. Kyerematen, O. Heinzerling, M. Degenhardt and G. Sadowski, *Mol. Pharm.*, **14**, 4374 (2017).
45. Lubrizol limited. Material safety data sheet (2018). https://www.lubrizol.com. Accessed 13 Apr 2022.
46. F. Meng, A. Trivino, D. Prasad and H. Chauhan, *Eur. J. Pharm. Sci.*, **71**, 12 (2015).
47. F. Qian, J. Huang, Q. Zhu, R. Haddadin, J. Gawel, R. Garmise and M. Hussain, *Int. J. Pharm.*, **395**, 232 (2010).
48. S. B. Teja, S. P. Patil, G. Shete, S. Patel and A. K. Bansal, *J. Excip. Food Chem.*, **4**, 1048 (2016).
49. T. T. Tran and P. H. Tran, *Pharmaceutics*, **12**, 745 (2020).
50. B. V. Eerdenbrugh and L. S. Taylor, *CrystEngComm.*, **13**, 6171 (2011).
51. T. Fornaro, D. Burini, M. Biczysko and V. Barone, *J. Phys. Chem. A*, **119**, 4224 (2015).
52. F. M. Iqbal, M. Ahmad and U. R. Tulain, *Acta Poloniae Pharm.*, **74**, 527 (2017).
53. X. Yuan, T. X. Xiang, B. D. Anderson and E. J. Munson, *Mol. Pharm.*, **12**, 4518 (2015).
54. S. Mohan, N. Sundaraganesan and J. Mink, *Spectrochim. Acta A*, **47**, 1111 (1991).
55. Z. Shang, L. Yang and G. Chang, *Polym. Int.*, **65**, 332 (2016).
56. N. Vijayan, R. R. Babu, R. Gopalakrishnan, P. Ramasamy and W. T. A. Harrison, *J. Cryst. Growth*, **262**, 490 (2004).
57. Y. Ishizuka, K. Ueda, H. Okada, J. Takeda, M. Karashima, K. Yazawa, H. Higashi, K. Kawakami, Y. Ikeda and K. Moribe, *Mol. Pharm.*, **16**, 2785 (2019).
58. L. A. Wegiel, L. J. Mauer, K. J. Edgar and L. S. Taylor, *J. Pharm. Sci.*, **102**, 171 (2013).
59. J. Dong, Y. Ozaki and K. Nakashima, *Macromolecules*, **30**, 1111 (1997).
60. H. Konno and L. S. Taylor, *J. Pharm. Sci.*, **95**, 2692 (2006).
61. Merck. IR Spectrum Table & Chart. https://www.sigmaaldrich.com/KR/ko/technical-documents/technical-article/analytical-chemistry/photometry-and-reflectometry/ir-spectrum-table. Accessed 24 Jan 2022.
62. U. Eduok, O. Faye and J. Szpunar, *RSC Adv.*, **6**, 108777 (2016).
63. J. A. Marks, L. A. Wegiel, L. S. Taylor and K. J. Edgar, *J. Pharm. Sci.*, **103**, 2871 (2014).
64. H. Honda, *Molecules*, **18**, 4786 (2013).
65. A. S. Tatton, T. N. Pham, F. G. Vogt, D. Luga, A. J. Edwards and S. P. Brown, *Mol. Pharm.*, **10**, 999 (2013).
66. Ü. Akbey, R. Graf, Y. G. Peng, P. P. Chu and H. W. Spiess, *J. Polym. Sci. B Polym. Phys.*, **47**, 138 (2009).
67. S. Ando, J. Kikuchi, Y. Fujimura, Y. Ida, K. Higashi, K. Moribe and K. Yamamoto, *J. Pharm. Sci.*, **101**, 3214 (2012).
68. F. Grifasi, M. R. Chierotti, K. Gaglioti, R. Gobetto, L. Maini, D. Braga, E. Dichiarante and M. Curzi, *Cryst. Growth Des.*, **15**, 1939 (2015).
69. E. Browne, Z. A. Worku and A. M. Healy, *Pharmaceutics*, **12**, 433 (2020).
70. D. S. Frank and A. J. Matzger, *Mol. Pharm.*, **15**, 2714 (2018).
71. Q. He, J. Liu, J. Liang, X. Liu, D. Tuo and W. Li, *Materials*, **11**, 247 (2018).
72. M. Monschke and K. G. Wagner, *Pharmaceutics*, **12**, 541 (2020).
73. N. G. Solanki, K. Lam, M. Tahsin, S. G. Gumaste, A. V. Shah and A. T. M. Serajuddin, *J. Pharm. Sci.*, **108**, 1453 (2019).
74. T. Swift, L. Swanson, M. Geoghegan and S. Rimmer, *Soft Matter.*, **12**, 2542 (2016).
75. V. Wilson, X. Lou, D. J. Osterling, D. F. Stolarik, G. Jenkins, W. Gao, G. G. Z. Zhang and L. S. Taylor, *J. Control Rel.*, **292**, 172 (2018).
76. M. O. Jara, Z. N. Warnken and R. O. Willams III, *Pharmaceutics*, **13**, 97 (2021).
77. E. L. McConnell, A. W. Basit and S. Murdan, *J. Pharm. Pharmacol.*, **60**, 63 (2008).

Supporting Information

Amorphous solid dispersions of tegoprazan and three different polymers: *In vitro/in vivo* evaluation of physicochemical properties

Paul Kim*, In-Seo Lee*, Ji-Yoon Kim*, Min-Jeong Lee, and Guang Jin Choi*,**,†**

*Department of Medical Science, Soonchunhyang University, Asan, Chungnam 31538, Korea
**Department of Pharmaceutical Engineering, Soonchunhyang University, Asan, Chungnam 31538, Korea
(*Received 10 June 2022 • Revised 11 August 2022 • Accepted 1 September 2022*)

Table S1. Physicochemical properties for each polymer

	Molecular weight (Mw) (Unit: Da)	Glass transition temperature (T_g) (Unit: °C)
HPMCAS	55,000-93,000 Da	Near 120
PVP	1,300,000 Da	150-180
Carbomer	700,000-4,000,000,000 Da	130-140

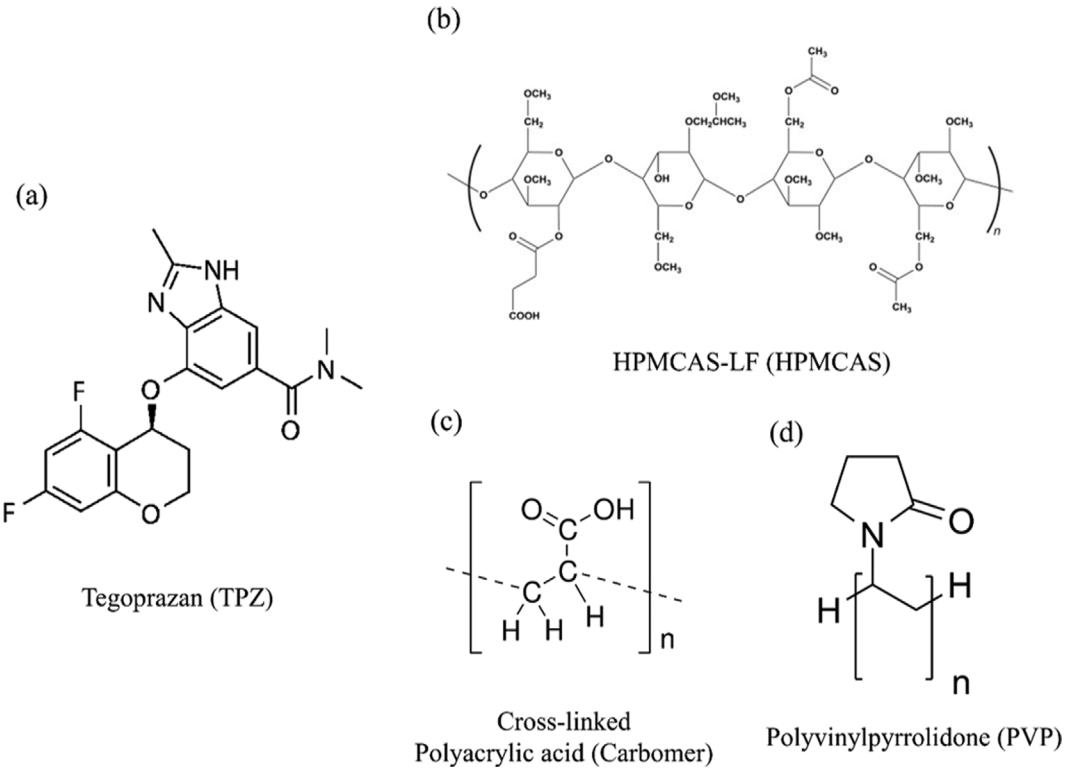

Fig. S1. Chemical structures of (a) Tegoprazan, (b) HPMCAS-LF, (c) Carbomer, and (d) Polyvinylpyrrolidone.

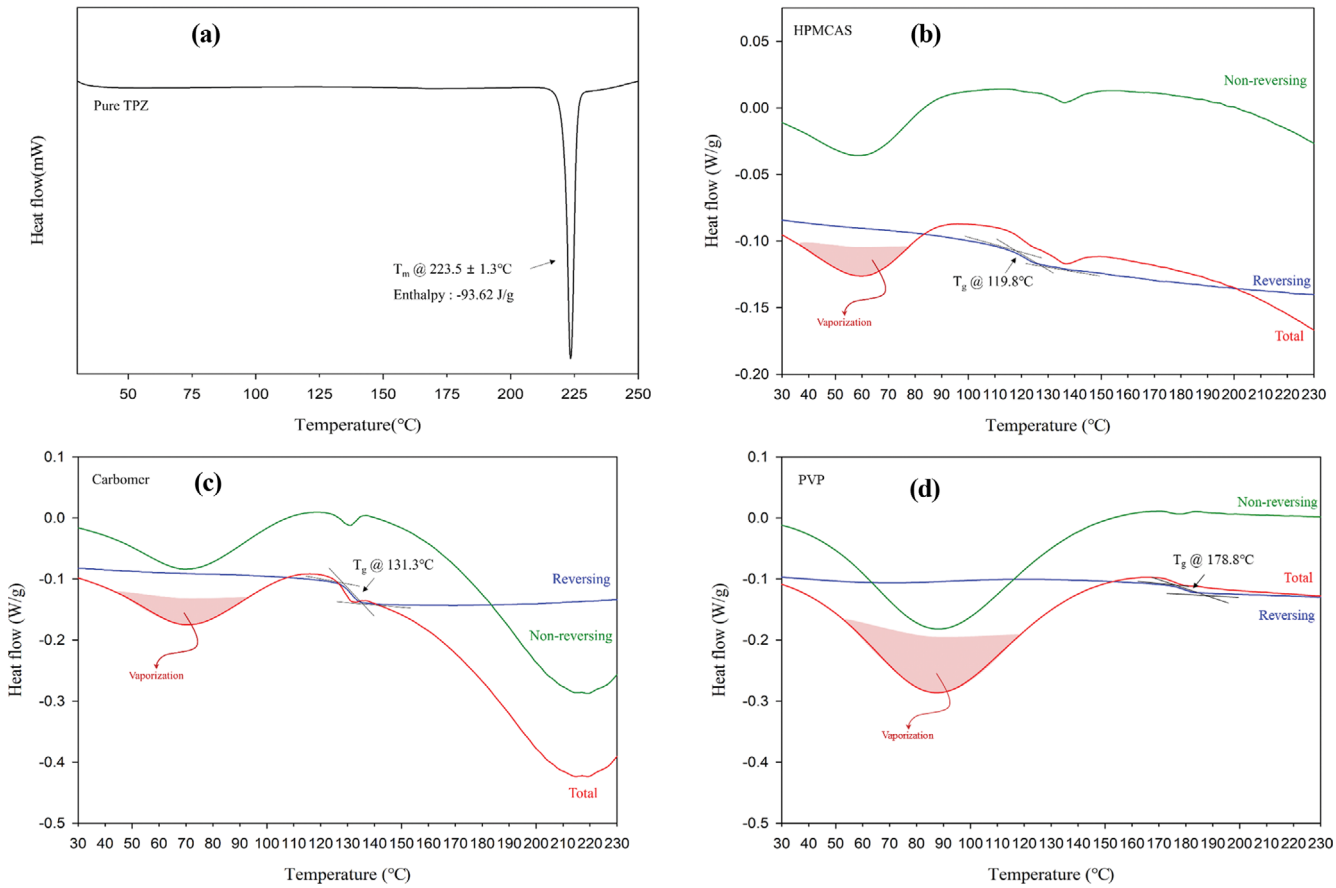

Fig. S2. MDSC thermograms of (a) Tegoprazan, (b) HPMCAS, (c) Carbomer, and (d) PVP.

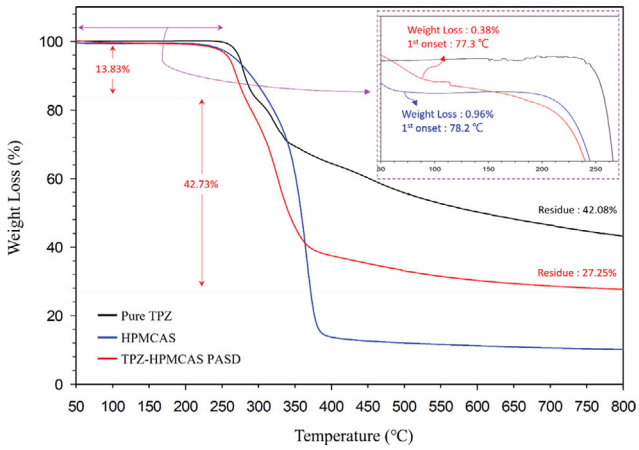

Fig. S3. MDSC thermograms of TPZ-HPMCAS PASD set.

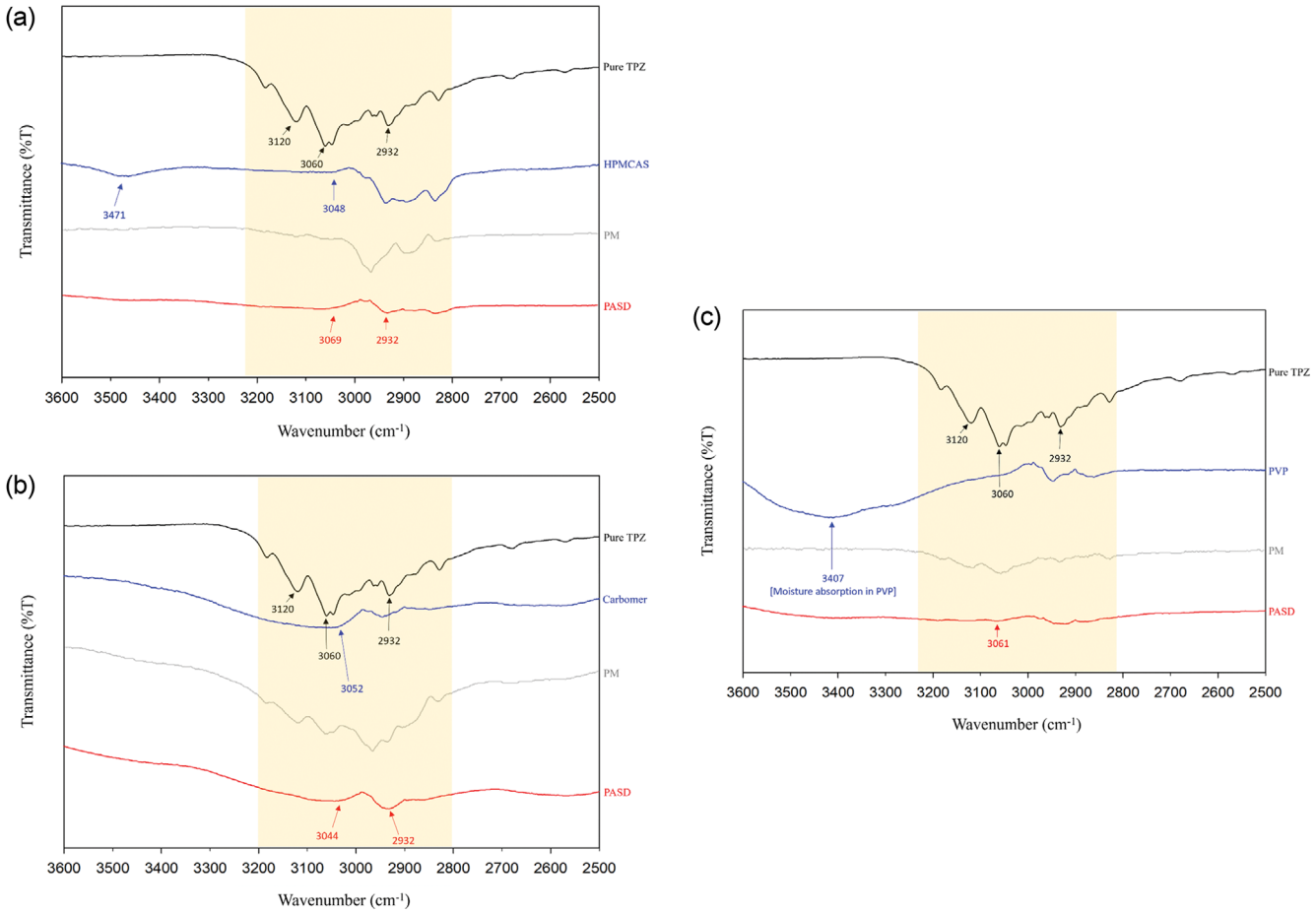

Fig. S4. IR spectra of (a) TPZ-HPMCAS, (b) TPZ-carbomer, (c) TPZ-PVP PASD materials: 3,600-2,500 cm^{-1} is for N-H bonding.

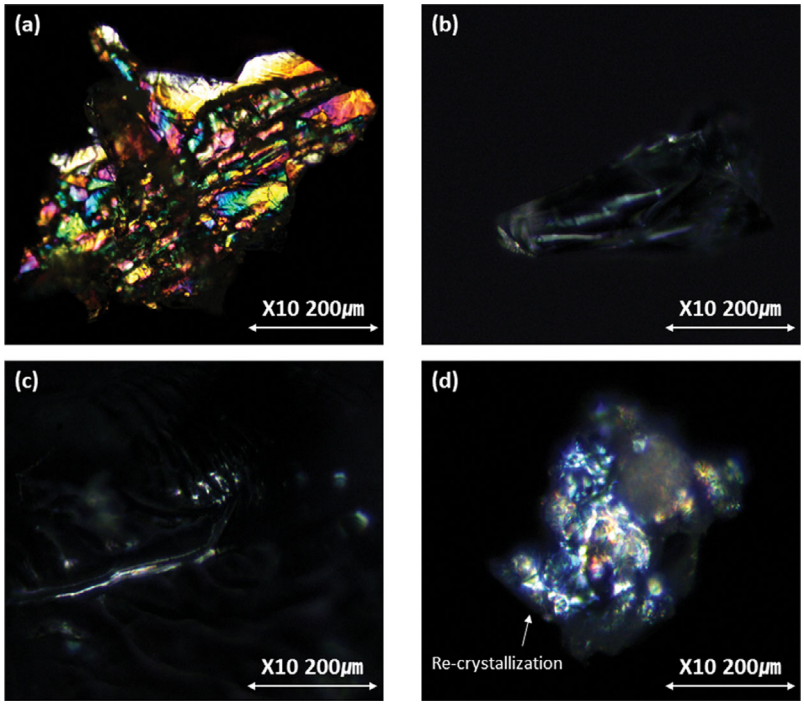

Fig. S5. PLM images of TPZ and PASDs powders; (a) crystalline form of TPZ at ×10, (b) TPZ-HPMCAS PASD at ×10, (c) TPZ-carbomer PASD at ×10, and (d) TPZ-PVP PASD at ×10.